9A.4 CHARACTERIZATION OF THE INTERNAL GRAVITY WAVE FIELD GENERATED BY A KATABATIC FLOW IN A DEEP VALLEY

Yann Largeron*, Chantal Staquet, Charles Chemel and Jean-Pierre Chollet

August 1, 2008

Abstract

Atmospheric circulation over complex terrain is governed by both synoptic forcing and thermal circulation induced by radiative heating or cooling of the ground surface. At night or in winter, when the synoptic forcing is weak enough, the dynamics of the atmospheric boundary layer in a deep valley is dominated by katabatic (down-slope) flows. Indeed, as soon as the ground surface is sloping, a horizontal temperature gradient is created between the air just above that surface and the ambient air, because of the differences between thermal capacity of the air and of the ground.

As predicted theoretically (e.g. [Fleagle (1950)], [McNider (1982)]) and shown from *in situ* measurements (e.g. [Helmis & Papadopoulos (1996)], [van Gorsel et al. (2004)], [Bastin & Drobinski (2005)]), oscillations in katabatic winds do occur along the slope. When the atmosphere is stably-stratified, the angular frequency of these along-slope oscillations is proportional to the Brunt-Väisälä frequency of the ambient atmosphere and to the sine of the slope angle.

Such an unsteady katabatic flow in a stably-stratified atmosphere must generate internal gravity waves. These waves are usually not resolved in mesoscale models. Whilst breaking, they induce mixing, which needs to be parameterized in such models. A preliminary high-resolution numerical investigation of the dynamics of the stably stratified atmosphere of a valley has suggested that the frequency of these waves is equal to about $0.8N$ ([Chemel et al. (2008)]), and so, is independent of the slope angle of the topography (unlike the pulsation of the katabatic wind). Theoretical work ([Voisin (2007)]) and previous laboratory experiments are consistent with this finding.

The aim of this study is to extend the characterization of the oscillations in the katabatic flow and of the internal gravity wave field emitted by this flow to a large range of stratification and slope angle values. To proceed, we have performed numerical simulations for an idealized topography of a deep valley with the ARPS meteorological model using a high resolution in space and time (down to 50 m horizontally, 4 m vertically with a time step of 0.2 s). In this paper, we discuss the mechanisms responsible for the along-slope oscillations and for the emission of the waves and we clarify how the wave frequency depends upon the stratification.

*Corresponding author: Yann Largeron, LEGI, BP 53, 38041 Grenoble cdx 9, France; e-mail: Yann.Largeron@hmg.inpg.fr

1 Introduction

In the absence of strong synoptic forcing, the flow in a narrow valley is driven by thermal circulations due to the heating or cooling of the soil surface. In regions of sloping ground surfaces, it is well-known that, at night or in winter, the cooling of the soil often induces down-slope, also referred to as katabatic, flows. If, moreover, the atmosphere is stably-stratified, the katabatic flow perturbs the stably-stratified air and internal gravity waves are generated.

According to *in situ* measurements ([Helmis & Papadopoulos (1996)], [Gryning et al. (1985)], [Princevac et al. (2008)], [van Gorsel et al. (2004)], [Bastin & Drobinski (2005)]), the katabatic flow is highly variable and intermittent. Temporal organization can still be detected, as temporal oscillations have been measured in these field campaigns. The existence of such oscillations was first accounted for by [Fleagle (1950)], invoking compressionnal warming as the catabatic wind flows down. The theoretical model thus derived was extended by [McNider (1982)] to a stably-stratified atmosphere, by adding buoyancy effects. McNider's model predicts that the oscillating period of the catabatic flow is $T = 2\pi/N\sin\alpha$, where N is the Brunt-Väisälä frequency (whose square is proportional to the ambient vertical potential temperature gradient) and α is the local angle of the topography with the horizontal. Very few studies dealt with the generation of the waves from the unsteadiness of the katabatic flow. A preliminary investigation was made numerically in an idealized alpine valley by [Chemel et al. (2008)]. This work shows that there are two oscillating systems in the stable boundary layer of a valley: one is associated with along-slope temporal oscillations in the katabatic wind as predicted by [McNider (1982)] while the other consists of the oscillations of the internal wave field in the whole atmospheric boundary layer. These conclusions are in good agreement with the observations made by [van Gorsel et al. (2004)] during the Riviera campaign. The study of [Chemel et al. (2008)] also led to the conclusion that the power spectrum of the internal waves is peaked at a frequency given by $\omega/N \approx 0.8$.

However, knowledge of the characteristics of these oscillating motions are missing. Especially, the effect of local parameters such as the value of the slope, the stratification of the atmosphere and the global topography of the valley should be addressed. This is the purpose of the present study.

To adress these questions, we analyse numerical simulations performed with the ARPS code. The setup of the simulations is described in the next section. Then, the general features of the flow is reported in section 3. The analysis of the oscillating motions is reported in section 4. Finally, we investigate the effect of the stratification in section 5. Conclusions are drawn in the final section.

2 Setup of the simulation

2.1 The numerical model

The numerical simulations are performed with the ARPS code (Advanced Regional Prediction System, Xue et al. (2000)). This is a non-hydrostatic atmospheric model appropriate for scales ranging from a few meters to hundreds of kilometers. The code solves the compressible Navier-Stokes equations that describe the atmospheric flow, and uses a generalized terrain-following coordinate system. Microphysical processes, surface layer physics and a soil model are included. Open boundary conditions are imposed for the velocity field in both horizontal directions. This field satisfies a no-slip condition on the topography while a Rayleigh sponge is imposed in the upper part of the domain. We model a 3 hour nocturnal winter situation starting at 22:00 UTC on December 21st at the latitude of an alpine valley. No velocity field is imposed at initial time and there is no synoptic forcing as well. The topography and initial temperature field are discussed below.

The Navier-Stokes equations are discretized in space with a centered fourth-order finite difference scheme on a staggered grid (of Arakawa C type). Time is discretized with a centered leapfrog time scheme, with a mode-splitting time integration technique for solving the acoustic waves. Three turbulence closure schemes are available in the code. Here, we use the classical 1.5 order turbulent kinetic energy (TKE) closure scheme.

The horizontal resolution is 200 m in both the x and y directions. Along the vertical direction, we use a variable grid, starting from 5 m in the first

100 m above the topography and slowly increasing upwards to reach 98 m at an altitude of 7000 m. The corresponding number of grid points is $121 \times 103 \times 140$. The time step is 0.25 s.

2.2 The topography of the valley

In the simulations, we use an idealized topography based on the analytical profile of a valley provided in [Rampanelli et al. (2004)]. Its expression is given by $z = h(x, y) = Hh_x(x)h_y(y)$ with $h_x(x) = 0.5(1 - \cos(\pi(|x| - V_x)/S_x))$ for $V_x < |x| < V_x + S_x$; for $|x| < V_x$, $h_x(x) = 0$ and for $|x| > S_x + V_x$, $h_x(x) = 1$. The function h_y is defined as $h_y(y) = 0.5(1 + \tanh(y/S_y))$.

The valley has a NS oriented axis and is open on a plain on the south boundary so that an along-valley wind can develop. The valley length is 20 km and the width $(2V_x)$ is 1240 m at the bottom level. The sloping sidewall width (S_x) is equal to 2640 m and the summits (H) are at the altitude of 1700 m. Figure 1 shows that the height of the summits varies along the valley axis, and so does also the value of the maximum slope angle in a vertical cross-section. This value ranges from around 3^o close to the plain to 44^o at the northern part of the valley.

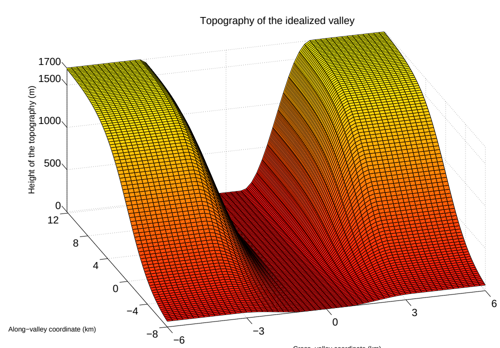

Figure 1: Topography of the idealized valley.

2.3 The initial temperature profiles

2.3.1 The initial atmospheric temperature field

We impose a vertical potential temperature profile $\theta(z)$ at initial time which has a value of 271K at the bottom of the valley and evolves linearly with height. The Brunt-Väisälä frequency $N = (g/\theta_0)(d\theta/dz)^{1/2}$ where θ_0 is a reference potential temperature is therefore constant. Note that due to topography, the absolute temperature at a given height above the soil surface is a function of x and y. The temperature of the soil surface is initialized with an offset from the temperature of the adjacent air. Here, we take an offset of 0^oC or 3^oC (see next sections for detail) which means that the initial *absolute* temperature of the soil surface is equal to, or 3^oC less than, the initial *absolute* temperature of the adjacent air. We also impose an offset between the soil surface and the deep soil (which is set to 0^oC or 5^oC in our simulations). This is not a forcing but just an initial condition. The temperature changes as time evolves in agreement with the thermodynamic laws prescribed by the code.

2.3.2 The soil surface temperature

A classical two-layer soil model is considered, with T_s being the soil surface temperature and T_2 the temperature of the deep soil. The temporal evolution of T_s is governed by the equation:

$$\frac{\partial T_s}{\partial t} = C_s(Rn - H - LE) + \frac{2\pi}{\tau}(T_s - T_2), \quad (1)$$

where Rn, H, and LE are the net radiative flux, the sensible heat flux and the latent heat flux respectively. The coefficient C_s is the heat capacity of the soil surface and τ is the duration of a day.

The typical evolution of T_s as time evolves is displayed in figure 2: the soil temperature varies by a few degrees per hour, consistent with *in situ* measurements by [Peck (1996)] for instance.

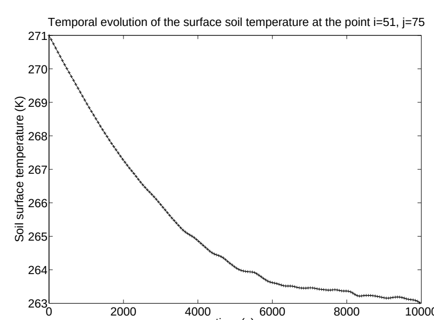

Figure 2: Temporal evolution of the soil surface temperature at a given point of the valley.

3 General behaviour of the stably-stratified atmospheric boundary layer in a deep valley

The purpose of this section is to provide a brief overview of the motions which develop in the atmosphere of the valley as a result of thermal forcing by the cooling of the soil and in the absence of synoptic forcing.

3.1 The katabatic wind

When cooling, the lower layers of the atmosphere become denser, and the cold air thus created flows down by gravity toward lower altitudes. Such a katabatic flow is visualized in figure 3, which displays an instantaneous vertical cross section of the contours of the vertical velocity at $y = +7$ km, where the maximum slope angle is $\simeq 44^o$. The maximum amplitude is of the order of 2 m/s, consistent with *in situ* measurements. Note that a katabatic wind also develops on the slopes that connect the summits to the plain, which is of much weaker amplitude.

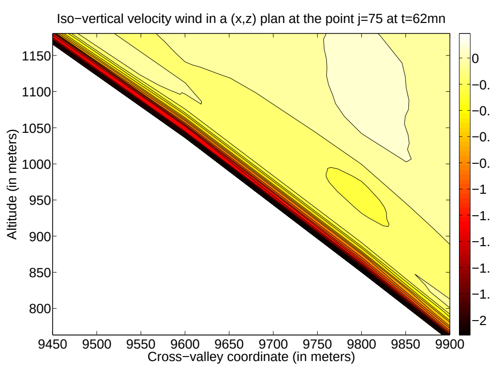

Figure 3: Katabatic wind flowing down the slope of the valley. Contours of the vertical velocity at $y = +7$ km at t=62 mn (the maximum slope angle is 44^o).

3.2 Internal gravity waves generated by the katabatic wind

Since the atmosphere is stably stratified, any non-horizontal time-varying disturbance radiates internal gravity waves. As mentioned in the Introduction and further discussed in Section 4.1, the katabatic wind is unsteady and therefore generates an internal gravity wave field which propagates in the whole valley and away from it because of the constant stratification.

Coriolis effects are very weak in the present case because the scales and velocities we consider are small (the Rossby number associated with the katabatic flow is $\simeq 100$ and that of the emitted waves, as shortly seen, is larger than 1). Therefore, Coriolis effects can be ignored in the following. As discussed in classical textbooks (for instance, [Lighthill (1978)]), the flow induced by plane internal gravity waves in the absence of Coriolis effects is a parallel shear flow, whereof velocity is directed along the planes of constant phase. The angle of these phase planes with the vertical, θ say, sets the wave frequency ω, when the Brunt-Väisälä is given. Indeed, from dispersion relation, one has : $\omega = N\cos\theta$.

The emission of internal gravity waves by the unsteady katabatic wind is illustrated in figure 4b by velocity vectors in a $y = +7$ km vertical plane : velocity vectors of alternate direction as one moves along the slope are indeed visible. Since the wave emission has just started (that is, the wave velocity is zero away from the slope), the wave pattern consists of closed cells of alternate sign along the slope. (Note that the vectors close to the slope, which are associated with the katabatic flow, have been suppressed for clarity.)

This cell structure clearly appears when the vertical velocity component is plotted in the same vertical plane (figure 4a). The figure also shows that the waves display a remarkable feature : the angle θ that the cell structures make with the vertical is the same whatever the emission location along the slope, despite the slope angle varies. This suggests that the wave frequency is constant, for a given N. This important feature will be further discussed in the next sections. The amplitude of the wave-induced velocity is 0.2 m/s, that is, ten times smaller than the vertical velocity of the katabatic flow which emits the waves. (Constant contours of the horizontal velocity component u also displays the same features, with a 0.5 m/s velocity).

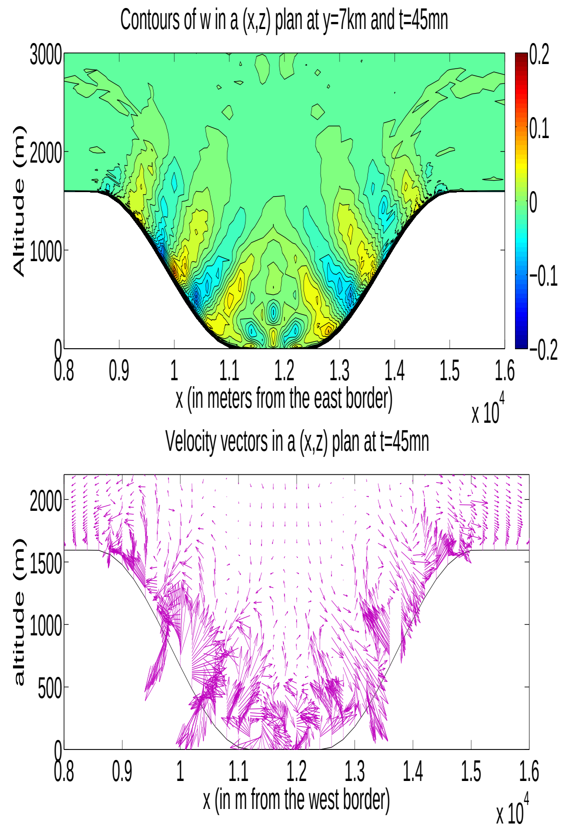

Figure 4: (a) Contours of the vertical velocity after 45mn of simulations at y=+7km. (b) Velocity vectors in a (x,z) cross section at y=+7 km after 45 *mn.*

3.3 The valley wind

A valley wind sets in which flows down to the plain (Figure 5). This valley wind is generated by the katabatic flow, from mass conservation, but is rather weak. It is noticeable that the wind is not generated at the bottom of the valley, but at an altitude around 1000 m, and reaches the bottom of the valley while flowing down.

4 Analysis of the case $N = 1.47\ 10^{-2}$ rad/s

We focus on a case for which the value of the stratification lies in the middle of the range of stratification we consider and is typical of those encountered in the atmosphere. Thus, the vertical temperature gradient is 6 K/km associated with

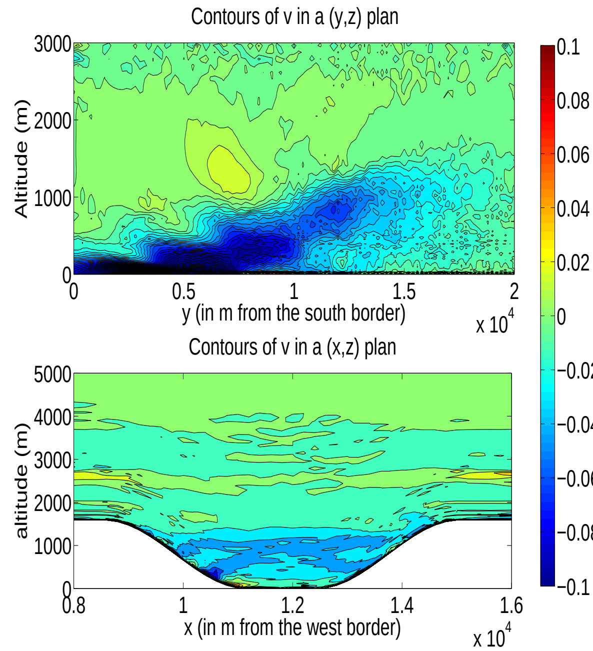

Figure 5: Top : Contours of v in a (y, z) section along the valley axis after 45 *mn of simulation. Bottom : Contours of v in a (x, z) section for y=* 15 *km (from south border) after* 45 *mn of simulation.*

$N = 1.47.10^{-2}$ rad/s.

4.1 The katabatic wind

4.1.1 Profile of the along-slope wind

We project the wind velocity on an axis s along the topography (see fig. 6) and compute the component thus obtained, u_s say, as a function of the coordinate normal to the topography n. The profil $u_s(n)$ is plotted in figure 7 at a given time, for $y = +7$ km (that is, in the narrow end of the valley) and at the point of maximum slope angle.
One can distinguish a lower part in which the wind is directed down the slope, over a thickness of roughly 50 m. The velocity reaches a maximum value of a few m/s around 10 m. Around 100 m above the ground, a return flow is present as a result of mass conservation: the wind is directed upward the slope. These observations agree well with *in situ* measurements of katabatic flows on steep slopes (larger than about 10^o), both from a qualitative and a quantitative point of view on a single slope (f.i. [Helmis & Papadopoulos (1996)],

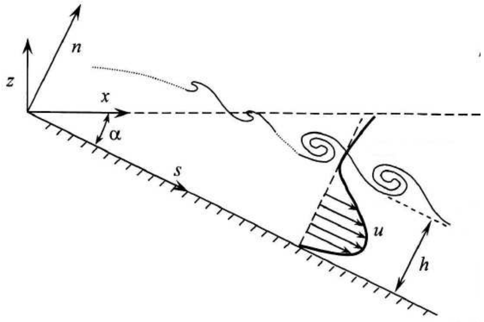

Figure 6: Definition of the sloping coordinate system (extracted and adapted from [Princevac et al. (2008)])

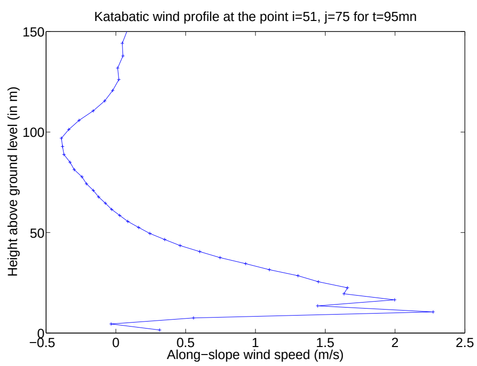

Figure 7: Along-slope component of the wind versus the coordinate normal to the topography n, in the middle of the slope ($x = +2$ km, $y = +7$ km

[Monti et al. (2002)], [Skyllingstad (2003)], Baines (2005)) or in a valley ([Gryning et al. (1985)], [van Gorsel et al. (2004)]).

4.1.2 Spatial dependency of the katabatic wind

The purpose of this section is to investigate the spatial dependency of the katabatic wind component u_s averaged over the 3 hours of simulation. We refer to this average velocity as $\langle u_s \rangle_t$. Figure 8 (top frame) displays $\langle u_s \rangle_t$ along the s-axis at $y = +7$ km at 1.5 m above the ground. The slope angle α is superimposed.

Three features should be noticed. First, the maximum value for $\langle u_s \rangle_t$ is not reached where α is maximum but about 500 m upstream. Second, the value of $\langle u_s \rangle_t$ is not symmetrical about the middle of the slope, whereas α is symmetrical about this point.

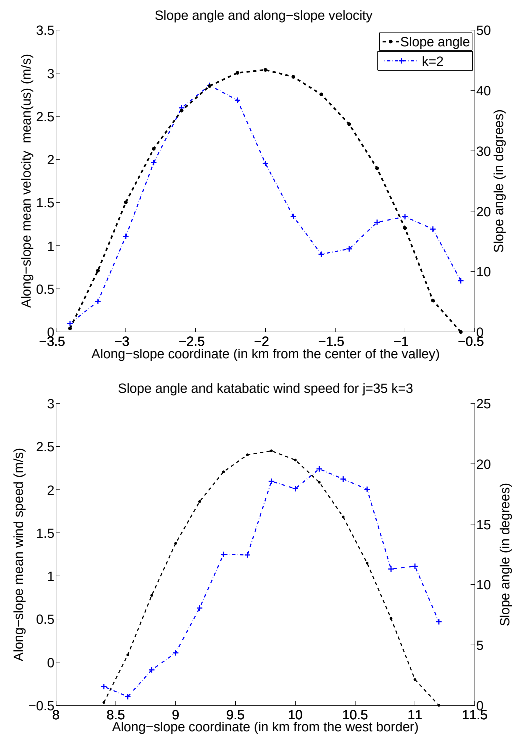

Figure 8: Top frame. Blue : Time average velocity component along the slope $\langle u_s \rangle_t(s, n = 1.5$ m, $y = +7$ km). Black : Slope angle α of the topography along the s-axis for $y = +7$ km. Bottom frame : same as top frame, for $y = -1$ km.

It therefore appears that the expression derived by [McNider (1982)] for the value of the average katabatic winds (namely $\langle u_s \rangle_t = L_c/(\gamma\ \sin\alpha)$ in which L_c is the cooling rate, γ the lapse rate and α the slope angle) is not directly applicable in this situation where the slope is not uniform. Finally, there is a localized region of weaker wind, implying that the wind loses momentum there. At this point, two processes may be invoked, which are the generation of either the internal wave field or the valley wind. Note (not shown) that this velocity deficit persists in the first few tens of meters above the ground while weakening.

This behavior does not persist when one moves along the valley axis. Figure 8 (bottom frame) shows indeed that, in the vertical plane located at $y = -1$ km, the momentum loss is no longer visible and the change in $\langle u_s \rangle_t$ is more symmetrical, with a slight shift toward the bottom of the slope very likely because of inertia.

The behavior described from this Figure is recovered when $\langle u_s \rangle_t(s, n, y)_t$ is plotted versus y for a given s and n (figure 9). Indeed, when the x-plane we consider coincides with the upper part of the slopes (top frame), $\langle u_s \rangle_t$ is roughly proportionnal to the slope angle. By contrast, for a value of s associated with the middle of the slopes (bottom frame), the figure shows that $\langle u_s \rangle_t$ first increases as the slope angle increases and then decreases in the upper narrow end of the valley, where the topography is very steep (having slope angles around 44^o).

Therefore it seems that the change in the katabatic wind along the slope is not the same when the angle of the slope varies, even if the curvature remains constant. This suggests that a physical process draws energy from the katabatic wind where the slopes are the highest (and longest) in the steepest areas of the topography, whereas this process does not exist (or is weaker) where the topography has a weaker slope.

Therefore if this physical process corresponds to the emission of internal gravity waves, the region of wave emission would be located in the middle of the slopes of the upper narrow end of the valley, where the slopes are the steepest, with a maximum angle close to 40^o.

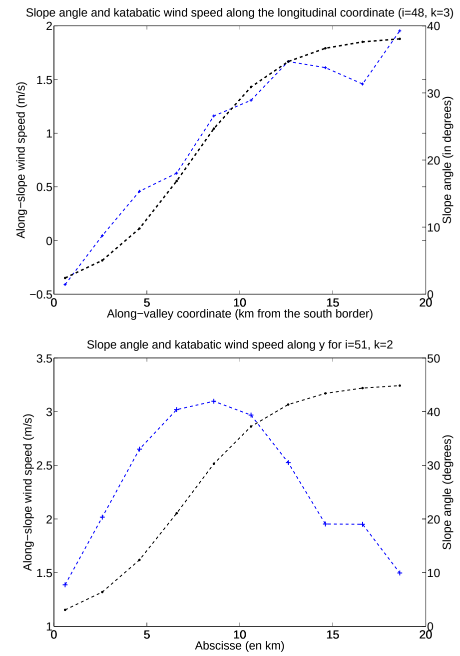

Figure 9: Blue : Evolution of $\langle u_s \rangle_t$ along the y-axis for a given value of x. Black : Evolution of the slope angle α along the y-axis for the same value of x. Top : $x = +2.6$ km; bottom : $x = +2$ km.

4.1.3 Temporal oscillations of the katabatic wind

At a given point of the slope, the amplitude of the component of the wind along the topography varies with time. According to theoretical analysis ([Fleagle (1950)], [McNider (1982)]), the adiabatic warming and the buoyancy force are the mechanisms responsible for these oscillations. The characteristic frequency of these oscillations is given by ([McNider (1982)]):

$$\omega_{McNider} = N \sin\alpha. \tag{2}$$

In the case we consider, the period of these oscillations is about 10 minutes at the locations where the slope is the highest, namely 44^o. Such oscillations can indeed be recorded there, as attested by Figure 10a (these oscillations exist all along the slope and can be better detected at the bottom of the slope). For layers of air very close to the ground, a power spectrum of the katabatic wind velocity shows that the oscillations do coincide with those predicted by McNider's model (fig. 10b).

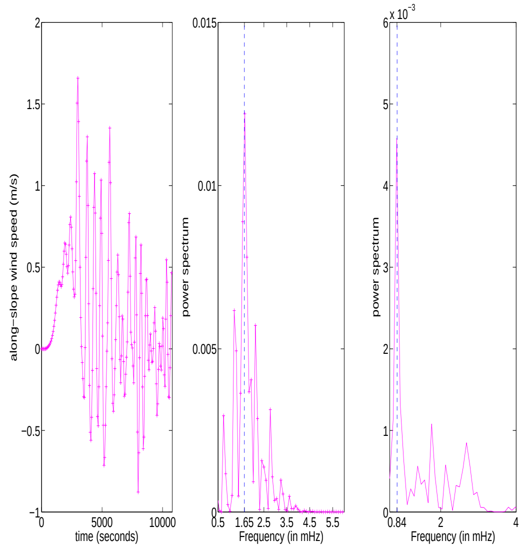

(a) (b) (c)

Figure 10: (a) Temporal evolution of u_s at x=0.8 km, y=+10 km. (b) Power spectrum of u_s at x=0.8 km, y=+10 km (blue : $\omega_{McNider}$ with $N = 1.4710^{-2}$ rad/s and $\alpha = 44^o$). (c) : Power spectrum of u_s at x=1.4 km, y=-1km (blue : $\omega_{McNider}$).

When moving to areas of the valley where the slope angle is smaller, the period of these oscillations become longer, in agreement with expression (2). This can be seen in figure 10c, where the velocity spectrum is plotted at a location where the maximum slope angle is 21^o. The period is equal to 20 mn.

Note however that the katabatic wind is not everywhere oscillating with the frequency $\omega_{McNider}$. The spectrum of the temporal variations of u_s most often exhibits several peaks around this frequency. This is possibly due to the fact that the slope of our valley is not uniform while the theoretical frequency $\omega_{McNider}$ is obtained for an infinitely long and uniform slope.

From the viewpoint of the structure of the katabatic winds, the McNider oscillations are especially representative of the temporal variations of the katabatic wind in the lower layers (less than $20-30$ m above ground). But the oscillations in the return flow around 100 m also have a quite similar frequency.

4.2 The internal wave field

4.2.1 Spatial structure of the waves

As discussed in Section 3.2, the katabatic wind generates internal gravity waves and this generation seems to occur more favourably on steeper slopes. As the waves propagate away from the slope, their phase lines take the form of cells, making an angle of approximately 45^o with the vertical (this point is further discussed in the next Sections).

The katabatic flow sets in during the first 20 minutes or so of the simulation. During this period, no wave is visible. After 20 minutes, fluid motions appear from the center of the valley up to the summits as if the atmosphere was unstable. Thus the wind is going upward in the center of the valley and downward above the summits. Since the atmosphere is stably-stratified however, no convection cell can form (unlike what would happen if the atmosphere were unstable) and local circulations appear in the vicinity of the slope, near the center part of the valley and close to the top. These motions are surmounted by return flow of opposite direction because of mass conservation.

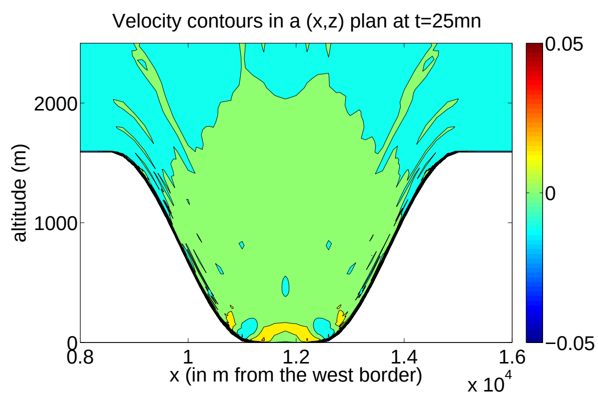

Figure 11: Contours of vertical velocity in a (x,z) plan after 25mn of simulation.

The front between the two katabatic flows eventually gives birth to a first cell that loops on itself because of the stratification, as shown in fig. 11. This occurs about 25 minutes after the beginning of the simulation.

After 45 minutes, the cell system is created all along the slope (see Fig. 4a). Waves are emitted from the slope and propagate away from it. We observe that

wave emission along the slope then occurs progressively for weaker slopes, as if wave emission were spreading along the direction of the valley axis, from steep to weak slopes.
Since the katabatic winds face each other, the waves they emit eventually yield a standing wave system forming at the bottom center part of the valley and progressively extending upward.

4.2.2 Wavelengths of the internal wave field

The structure of the wave field can be studied more precisely by computing so-called "Hövmoller" diagrams, which are simply plots of constant contours of a velocity component (or of the temperature) of the wave field, the axis being one spatial coordinate, x_i say, and time. The diagram can yield the phase speed in the direction of x_i from the slope of the contours as well as the wave frequency so that the wave length in the x_i direction can be inferred. Contours of the vertical velocity in a (y, t) diagram are thus plotted in figure 12 along the line defined by $x = -0.2$ km (close to the valley center) and $z = 400$ m, for the first one hour or so of the simulation. The figure shows that the waves reach this altitude after about half an hour and that the slope is infinite for y larger than 0.6 km (from south border). Hence, in the Northern part of the valley, the phase speed along the y direction vanishes: the wave structure may be assumed to be two-dimensional there namely, the waves propagate in the (x, z) plane.

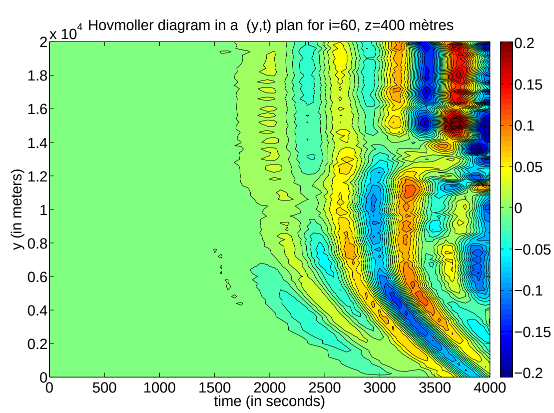

Figure 12: Contours of vertical velocity in a (x, t) diagram at $x = -0.2$ km and $z = 400$ m.

Contours of the vertical velocity in a (z, t) diagram along the vertical line defined by $x = 0.6$ km (close to the valley center) and $y = +9km$ (close to the Northern border) are plotted in figure 13. As above, phase lines are clearly visible, with a well defined slope during the first hour. The wave period T is given by the distance along the horizontal axis between two maxima and the phase speed c_z is equal to the value of the slope. We find $T \approx 10$ mn and $c_z = -2.5$ m/s so that, from the relation $c_z = \omega/k_z = \lambda_z/T$, one gets $\lambda_z \approx 1300$ m.

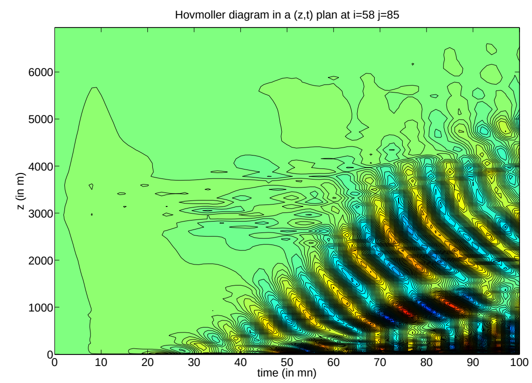

Figure 13: Contours of vertical velocity in a (z, t) diagram at $x = 0.6$ km and $y = +9$ km.

If we plot this Hövmoller diagram for a smaller value of y, where the slope is shallower, we get roughly the same phase speed and period.
To compute the wavelength along the x-direction, we plot the (x, t) Hövmoller diagram in the Northern part of the valley (so that no $y-$dependency may be assumed) and for $z = 800$ m (figure 14). At that altitude, the $x-$axis is limited to a range of values set by the topography. Waves do not attain this altitude before $t \simeq 2000-3000$ s and the phase lines then organize along well defined structures which are symmetric with respect to the valley axis. The formation of a standing wave system is visible at later times. The slope of the phase lines is $c_x \simeq 2.3$ m/s while the period is estimated to $\simeq 11$ mn, consistently with the computation from the (z, t) diagram. Using $c_x = \lambda_x/T$, we get $\lambda_x \approx 1400$ m.

4.2.3 Frequency analysis of the waves

We have computed the frequency of the waves from time series recorded at one point. In this section, we analyse how the wave frequency varies along

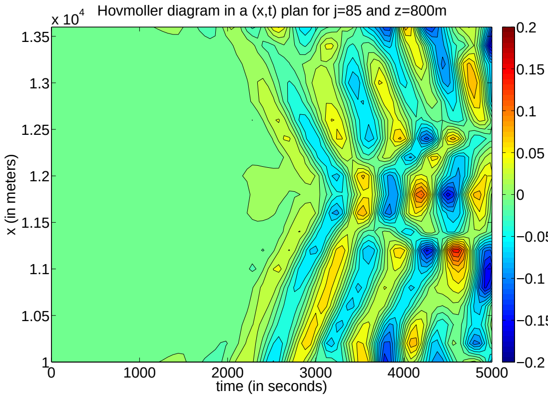

Figure 14: Contours of vertical velocity in a (x,t) diagram at $y = +9$ km and $z = 800$ m.

the vertical direction (that is, as the waves propagate away from the slope), along the valley axis and along the x-direction.

• *Change in the wave frequency along the vertical direction*

The frequency spectrum of the vertical velocity has been computed at different altitudes, ranging from 1000 m above the ground to approximately 2300 m above the ground, at a location in the valley where the slope is weak. The result is displayed in figure 15. The Brunt-Väisälä frequency is indicated with a red line and the frequency predicted by McNider at this location is shown with a blue line.

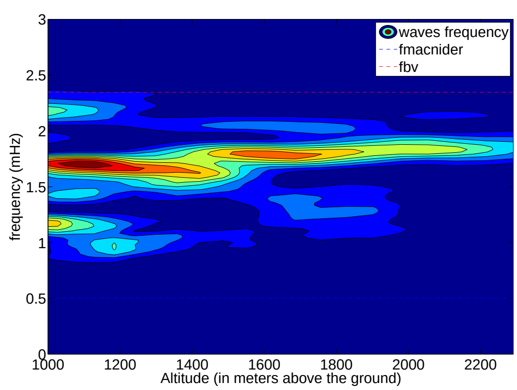

Figure 15: Evolution of the wave frequency with z. Red line : Brunt-Väisälä frequency N. Blue : frequency predicted by McNider.

Several frequencies are excited at lower altitudes but, from a distance to the ground larger than 1500 m, a single wave frequency is detected, which is quite different from McNider's frequency.

This behavior is recovered where the topography is steeper, with the frequency detected at high altitude being closer to McNider's frequency because of the higher slope.

This analysis therefore shows that the frequency of the waves at a distance from ground level greater than 1500 m can be assumed to be constant when moving along the vertical axis.

• *Change in the wave frequency along the valley axis*

We now analyse the change in the wave frequency along the valley axis. This is an important point since the slope of the topography varies along the valley axis. Hence, this analysis should allow us to determine whether the wave frequency depends upon that slope, as the McNider's frequency does. To get a closer comparison with the latter frequency, we also display $\omega_{McNider}$ on the same figure. The ratio ω/N is thus plotted versus y in figure 16, along with the ratio $\omega_{McNider}/N$=sinα. We take for α the maximum value of the slope angle in each plane y =constant.

The figure shows no clear dependency of ω versus y that is, with the slope of the topography. Hence, the wave frequency does not follow McNider's frequency. The wave frequency is comprised between 0.7 and 0.9 times the Brunt-Väisälä frequency so that a law of the form $\omega = 0.8.N$ may be assumed.

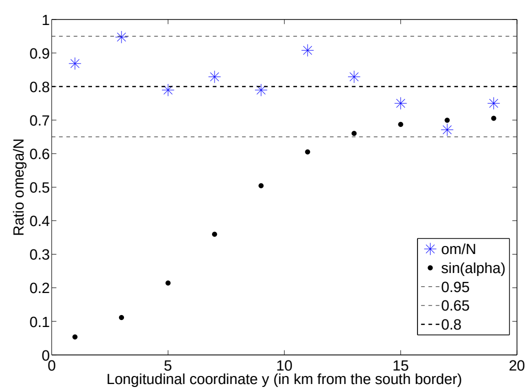

Figure 16: Blue symbols: Ratio ω/N versus y. Black : Ratio $\omega_M cNider/N$ versus y.

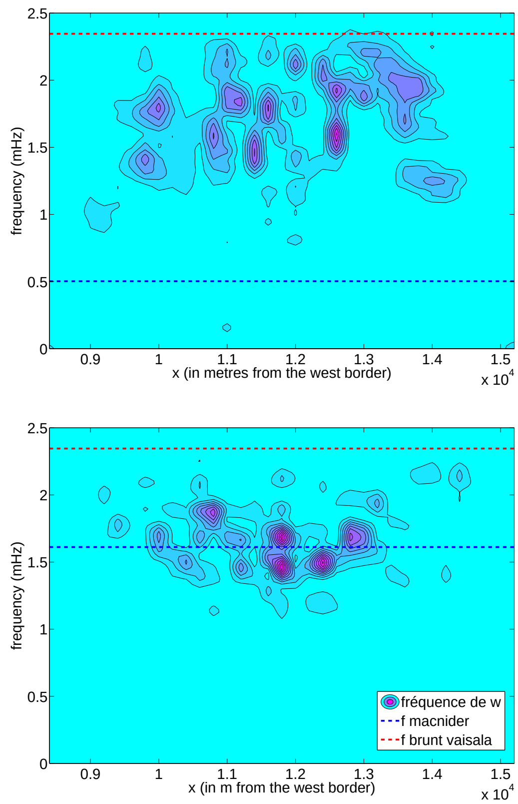

Figure 17: Evolution of the frequency with x for y=-3km (top frame) and y=+7km (bottom frame). Red dashed line: Brunt-Väisälä frequency N. Blue dashed line: frequency predicted by McNider.

- *Change in the wave frequency along x*

The dependency of the wave frequency as a function of x is eventually investigated for a given altitude ($z = 2200$ m), at two positions along the valley axis. For this purpose we plot ω versus x in figure 17 for $y = -3$ km (top frame) and $y = +7$ km (bottom frame). At the first location, frequencies are well distinct from McNider's frequency, as already found, and centered about a mean value equal to $0.75N$. At the second location, the frequency coincides to McNider's location due to the sine of the slope being equal to 0.8.

5 Influence of the thermal stratification

In order to investigate the effect of the stratification, we performed 8 simulations with different values of the Brunt-Väisälä frequency, ranging from 9.10^{-3} rad/s to $2.3.10^{-2}$ rad/s.
In agreement with the result displayed in figure 16, we found that the wave frequency is nearly independent on the slope (or equivalently on y). Indeed, we obtained the same figure as figure 16 in every simulation.
The measure of a frequency in a given point of the valley is marred with uncertainties due for example to the short time of the simulation - 3 hours - which leads to an uncertainty in the calculation of the frequency spectrum of approximately 0.24 mHz. According to figure 17, the frequency takes a value comprised between 0.65N and 0.95N along the y-direction. In the following, we assume that the frequency is nearly constant along y and compute its average value in y for each value of N, at a given (x, z) location. The $y-$average is referred to as $\langle\omega\rangle_y$ and is plotted versus N in figure 18 (top frame).
The figure shows that $\langle\omega\rangle_y$ increases with N, consistently with previous finding (where we have $\omega \simeq 0.8N$). To get the coefficient between $\langle\omega\rangle_y$ and N, the ratio $\langle\omega\rangle_y/N$ is displayed versus N in figure 18 (bottom frame).
This figure confirms the results of the detailed study of Section 4, namely that the frequency of the waves ranges between 0.7 and 0.85N. However, it contains an additional information: the ratio ω/N is constant and around 0.8 for weak stratification and seems to decrease linearly with N when the stratification becomes stronger. Further work is needed to analyze this behavior.

6 Conclusions

The purpose of this analysis was to revisit and extend the preliminary study performed by [Chemel et al. (2008)], on the emission of internal gravity waves by a katabatic flow. The study of [Chemel et al. (2008)] focused on caracterizing both the oscillations in the katabatic flow and the internal gravity wave field. A single computation was considered.

The present study confirms that two oscillating systems coexist, consisting in oscillations of the katabatic flow as predicted by [McNider (1982)] and in internal gravity waves with frequency $\simeq 0.8N$. The novelty here is to analyse the chronology and formation of the wave emission. Thus the waves first form at the bottom of the steepest slopes, which seems to be confirmed by the preliminary experimental study performed by Hazewinkel in 2006 (research training, Woodshole Summer School). The waves next form all along that slope and, subsequently, all along the other slopes along the valley axis.
Since the angle of the steepest slope is 44^o, the wave frequency incidentally coincides with McNider's frequency there. One may therefore wonder whether the wave frequency is not imposed by McNider's frequency, the wave system being then transported in some way throughout the valley. Preliminary study with a topography where the slope is everywhere equal to 30^o (so that the sine of the slope angle is smaller than 0.8) shows that waves with frequency close to $0.8N$ are still emitted.
We also ran eight simulations with different values of N and recover the $\omega \simeq 0.8N$ law. This ratio between the wave frequency and N may be explained by the theoretical work of [Voisin (2007)]. This work shows that the power of the waves radiated by an oscillating sphere or cylinder displays a maximum value for an oscillating frequency close to $0.8N$. The idea, proposed by Voisin, is that an unsteady flow, such as a katabatic wind, emits waves at any frequency, among them those having a frequency close to $0.8N$ are the most powerful and eventually dominate the wave signal. Laboratory experiments of localized turbulence in a stably stratified fluid are fully consistent with this result, reporting the emission of waves making an angle around 45^o with the vertical ([Wu (1969)], [Cerasoli (1978)]).

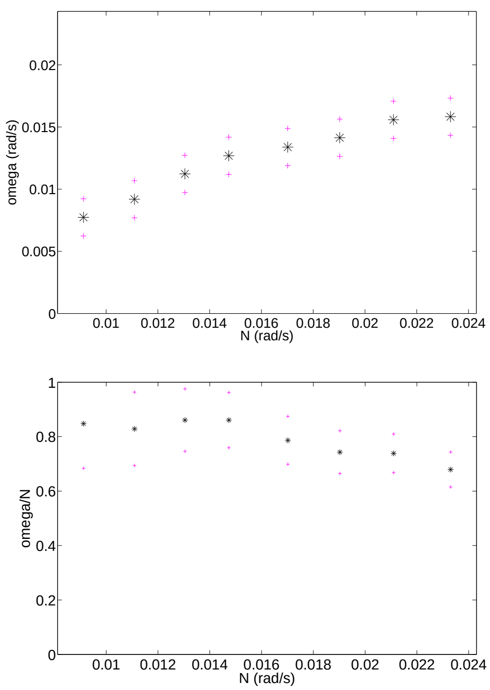

Figure 18: Top frame. Black symbols: $\langle\omega\rangle_y$ versus N. Magenta symbols: Uncertainties on the values plotted. Bottom frame. $\langle\omega\rangle_y/N$ versus N. Magenta : Uncertainties on the values plotted.

ACKNOWLEDGMENTS

Financial support from the IDAO/LEFE program of INSU and from the Cluster Environnement of the Région Rhône-Alpes is greatly acknowledged. All computations have been performed on the french computer center IDRIS operated by CNRS.

References

[Baines (2005)] Baines P.G. 2005: Mixing regimes for the flow of dense fluid down slopes into stratified environments. *J. Fluid Mech.*, **538**, 25-267.

[Bastin & Drobinski (2005)] Bastin S. and Drobinski P. 2005: Temperature And Wind Velocity Oscillations Along a Gentle Slope During Sea-Breeze Events. *Boundary-Layer Meteorology*, **114**(3): 573.

[Chemel et al. (2008)] Chemel C., Staquet C. and Largeron Y. (2008) Generation of internal gravity waves by a katabatic wind in an idealized alpine valley. *Submitted to Meteor. Appl. Physics.*

[Cerasoli (1978)] Cerasoli C.P. 1978: Experiments on buoyant-parcel motion and the generation of internal gravity waves, *J. Fluid Mech.*, **86**, 247–271.

[Fleagle (1950)] Fleagle R.G. (1950): A theory of air drainage, *J. Meteor.*, **7**, 227–232.

[van Gorsel et al. (2004)] van Gorsel E., Vogt R., Christen A. and Rotach M. 2004: Low frequency temperature and velocity oscillations in katabatic winds. *International Conference on Alpine Meteorology*, Brig, May 19 to 23, 2003.

[Gryning et al. (1985)] Gryning S.-E., Mahrt L. and Larsen S. 1985: Oscillating nocturnal slope flow in a coastal valley, *Tellus*, **37**A, 196-203.

[Helmis & Papadopoulos (1996)] Helmis C.G. and Papadopoulos K.H. 1986: Some aspects of the variation with time of katabatic flow over simple slope, *Quart. J. Roy. Meteor. Soc.*, **122**, 595-610.

[Lighthill (1978)] Lighthill J. 1978: Waves in Fluids (Cambridge University Press, 1978).

[McNider (1982)] McNider R.T. 1982: A note on velocity fluctuations in drainage flows. *J. Atmos. Sci.*, **39** (7), 1658-1660.

[Monti et al. (2002)] Monti P., Fernando H.J.S., Princevac M., Chan W.C., Kowalewski T.A. and Pardyjak E.R. 2002: Observations of flow and turbulence in the nocturnal boundary layer over a slope. *J. Atmos. Sci.*, **59**, 2513–2534.

[Peck (1996)] Peck L.: Temporal and spatial fluctuations in ground cover surface temperature at a Northern New England site. *Atmospheric Research*, **41**, 131–160.

[Princevac et al. (2008)] Princevac M., Hunt J and Fernando H.J.S.: Quasi-Steady Katabatic Winds on Slopes in Wide Valleys: Hydraulic Theory and Observations. *J. Atmos. Sci.*, **65**, 627–643.

[Rampanelli et al. (2004)] Rampanelli G., Zardi D. and Rotunno R. (2004): Mechanism of up-valley winds. *J. Atmos. Sci.*, **61**, 3097-3111.

[Skyllingstad (2003)] Skyllingstad E.D. (2003): Large eddy simulations of katabatic flows. *Boundary Layer Met.*, **106**, 217-243.

[Voisin (2007)] Voisin B. 2007: Added mass effects on internal wave generation. *Fifth International Symposium on Environmental Hydraulics*, Tempe, AZ, USA, 4–7 decembre 2007.

[Wu (1969)] Wu J. 1969: Mixed region collapse with internal wave generation in a density-stratified medium, *J. Fluid Mech.*, **35**, 531–544.

[Xue et al. (2000)] M. Xue, Droegemeier K. K. and Wong V. 2000: The Advanced Regional Prediction System (ARPS) – A multi-scale non hydrostatic atmospheric simulation and prediction model. Part I: Model dynamics and verification, *MAP*, **75**,161-193.